Channel Modeling and Performance Analysis of Airplane-Satellite Terahertz Band Communications

Joonas Kokkoniemi, *Member, IEEE*, Josep M. Jornet, *Senior Member, IEEE*, Vitaly Petrov, *Member, IEEE*, Yevgeni Koucheryavy, *Senior Member, IEEE*, and Markku Juntti, *Fellow, IEEE*

***Abstract*—Wireless connectivity in airplanes is becoming more important, demanded, and common. One of the largest bottlenecks with the in-flight Internet is that the airplane is far away from both the satellites and the ground base stations during most of the flight time. Maintaining a reliable and high-rate wireless connection with the airplane over such a long-range link thus becomes a challenge. Microwave frequencies allow for long link distances but lack the data rate to serve up to several hundreds of potential onboard customers. Higher bands in the millimeter-wave spectrum (30 GHz–300 GHz) have, therefore, been utilized to overcome the bandwidth limitations. Still, the per-user throughput with state-of-the-art millimeter-wave systems is an order of magnitude lower than the one available with terrestrial wireless networks. In this paper, we take a step further and study the channel characteristics for the terahertz band (THz, 0.3 THz–10 THz) in order to map the feasibility of this band for aviation. We first propose a detailed channel model for aerial THz communications taking into account both the non-flat Earth geometry and the main features of the frequency-selective THz channel. We then apply this model to estimate the characteristics of aerial THz links in different conditions. We finally determine the altitudes where the use of airplane-to-satellite THz connection becomes preferable over the airplane-to-ground THz link. Our results reveal that the capacity of the airborne THz link may reach speeds ranging from 50–150 Gbps, thus enabling cellular-equivalent data rates to the passengers and staff during the entire flight.**

***Index Terms*—Airplane communications, satellite communications, THz channel modeling, THz communications.**

I. Introduction

TODAY, terahertz (THz, 0.3 THz–3 THz) communication is widely considered to be one of the next frontiers for future wireless systems. Data transmission over the THz band offers at least an order of magnitude higher rates than emerging millimeter-wave (mmWave, 30 GHz–300 GHz) communication systems and two orders of magnitude when compared to state-of-the-art microwave solutions [1], [2]. Hence, THz communication cannot only exceed the performance requirements for the fifth-generation (5G) networks, but also enable many tempting applications in the area of holographic communications, augmented and virtual reality, and tactile internet [3]. While the first prototypes of point-to-point connections over the low THz frequencies are already appearing [4], the research community is slowly switching its focus on studying the features of THz links in prospective application-specific setups.

One of the attractive usage scenarios in the area is enabling THz connectivity with flying airplanes. The aviation industry has been growing by over 6% a year over the recent decades, reaching an incredible figure of 4.3 billion passengers carried in 2018 [5]. Although the current COVID-19 pandemic is momentarily slowing down the development, in the long run the trend is expected to continue. While the average duration of a flight is less than 3 hours, a substantial amount of flights are longer than 7 hours. Some flights between the continents take the even longer time up to enormous 18 hours 45 minutes with a recently introduced route between Singapore and Newark, USA, by Singapore Airlines. Despite the continuously increased popularity of long haul flights, the airplane is one of the few typical locations where the average person is used to not have high-rate Internet connectivity.

Aiming to address this limitation, modern aircrafts are already equipped with satellite-based solutions operating in Ku (12–18 GHz) and, recently, Ka (26.5–40 GHz) frequency bands. Still, these systems can provide only limited service to restricted numbers of passengers, as the aggregated traffic from over 400 users (e.g., in a Airbus A350-1000) cannot be efficiently multiplexed into a single mmWave link. Here, the use broadband THz spectrum provides decisive advantages, rapidly increasing the data rate of the airplane connectivity and thus allowing all the passengers and crew members to stay continuously connected to their common applications and services. However, the high-rate airborne connectivity in the THz band requires not only the evolution in the transceiver and antenna design. Importantly, it also demands a better understanding of the properties of the THz signal when propagating through the atmosphere at a high altitude. Potentially high losses at a multi-kilometer THz link between the airplane and a satellite may even question the

Manuscript received September 13, 2020; revised January 2, 2021; accepted January 28, 2021. Date of publication February 10, 2021; date of current version April 2, 2021. This work was supported in part by the Horizon 2020, European Union's Framework Programme for Research and Innovation, under Grant Agreement Nos. 761794 (TERRANOVA) and 871464 (ARIADNE), in part by the Academy of Finland 6Genesis Flagship under Grant 318927, and in part by the US Air Force Research Laboratory Grant FA8750-20-1-0200. The review of this article was coordinated by Prof. J. Joung. *(Corresponding author: Joonas Kokkoniemi.)*

Joonas Kokkoniemi and Markku Juntti are with the Centre for Wireless Communications, University of Oulu, Oulu 90014, Finland (e-mail: joonas.kokkoniemi@oulu.fi; markku.juntti@oulu.fi).

Josep M. Jornet is with the Department of Electrical and Computer Engineering, Northeastern University, Boston, MA 02115 USA (e-mail: jmjornet@northeastern.edu).

Vitaly Petrov was with the Tampere University, Tampere 33720, Finland. He is now with Nokia Bell Labs, Espoo 02610, Finland (e-mail: vitaly.petrov@tuni.fi).

Yevgeni Koucheryavy is with the Unit of Electrical Engineering, Tampere University, Tampere 33720, Finland (e-mail: yk@cs.tut.fi).

Digital Object Identifier 10.1109/TVT.2021.3058581

feasibility of the airborne THz communications. It will be shown in the numerical results that the THz bands have very potential for high altitude satellite communications. However, those require very large antenna gains and terrestrial communications benefits from lower losses at mmWave bands. In the case of, e.g., handheld applications where antenna gain at the user end is very low, the low frequency solutions are most likely the only feasible solution. That is, the feasibility of the high frequency systems depend on the application. High bandwidth applications will always benefit from the higher bandwidths offered by mmWave and THz communications with the latter having potential to provide the extreme data rates, but only in low loss situations.

Related Work

A general model for free-space wireless communications in the THz band was first presented in [6]. The model enables estimating the path loss over a direct THz link, properly accounting for the specific effects present in THz communications, such as molecular absorption. The properties of the THz propagation in complex environments have been extensively studied via ray-based simulations [7]–[10]. For this purpose, deterministic channel models are first built following the exact geometry of the scenario. Then, the impact of multipath propagation is modeled following either *ray-tracing* or *ray-launching* approach. The approach is featured by high accuracy but limited scalability, as even the minor modifications in the modeled scenario requires a restart of the computationally complex ray-based simulations. In response to this issue, mathematical approaches to model multi-path THz communications have been proposed in [11] and [12]. These stochastic models primarily target indoor THz systems, where the signal can reflect from walls and other obstacles multiple times before reaching the target receiver.

Despite the progress in understanding the key features of the THz signal propagation, the airborne nature of the THz links between an airplane and a satellite has its own specifics that must be taken into account in channel modeling. The topic has been partially covered in prior works. A simulation-based model for THz band satellite links has been proposed in [13]. Later, a review of weather impact on outdoor THz links has been presented in [14]. The latter study has been complemented by Y. Balal and Y. Pinhasi in [15], where effects of the atmosphere non-homogeneous refractivity on mmWave and THz band satellite links has been explored.

In parallel to academic research, some initial steps towards characterizing the airborne THz links have been made by International Telecommunication Union (ITU). Specifically, the approach to estimate the signal attenuation by atmospheric gases has been presented in ITU-R P.676-9 [16] while the noise levels for different frequencies (including the THz band) have been estimated in ITU-R P.372-13 [17].

Finally, one of the closest models to our approach – the am atmospheric model – has been presented by S. Paine from Smithsonian Astrophysical Observatory in [18]. The model first characterizes the absorption losses at different altitudes and then allows the estimation of the average effect when propagating through several atmospheric layers by integrating the obtained data. There are also other models suitable for THz band line-by-line absorption loss calculations, such as MODTRAN [19] and ATM [20]. However, as these have not been designed for wireless communications, they are not very agile for dynamic loss calculations as a function of a position of a moving network nodes. Still, these models are very accurate, but best suited for static link calculations. For dynamic environments and user nodes, it is more efficient to create a model that automatically calculates the path losses and the link budget based on the positions of the network elements.

Our Motivation and Contribution

Summarizing the related work survey, no model has been proposed to date for airborne THz band communications that takes into account: (i) the curvature of the atmosphere and, consequently, (ii) the non-uniformity of atmospheric absorption losses. Simultaneously, there has not yet been presented a detailed numerical study investigating the feasibility of airborne wireless communications via the THz band while accounting for the above-mentioned specifics. We aim to partially fill the gap in this article.

The main contributions of this article are thus:

1) The mathematical model to characterize the airborne THz band communications is proposed, taking into account (i) the features of the target use case and the deployment geometry, (ii) the peculiarities of the signal propagation through the atmosphere, as well as (iii) the prospective characteristics of THz radio equipment to operate in the airborne scenarios.
2) The illustrative numerical study is performed estimating the performance of the data exchange between an airplane and a satellite over the THz frequencies. Particularly, the signal-to-noise ratio (SNR) and the mean capacity of the airborne THz link are estimated. Our numerical study allows to conclude that capacities of 50–150 Gbps in airborne THz links can be achieved using certain sub-bands in the THz spectrum.

The remainder of this paper is organized as follows. In Section II we detail the system model used in our study. The specifics of the THz signal propagation are discussed in detail in Section II-B. The channel model for airborne wireless communications in the THz band is introduced in Section III. We later apply the contributed model in Section IV for the received signal quality and performance evaluation of prospective airborne THz links. The obtained analytical results are numerically elaborated in Section V. The concluding remarks are drawn in the last section.

II. System Model

A. Scenario Description

The general system concept is to provide high data rate fronthaul connection to an airplane, which furthermore serves the passengers on board and in general provides Internet connection to the airplane. However, as a side product, the channel models derived in this paper cover several use cases for aerial

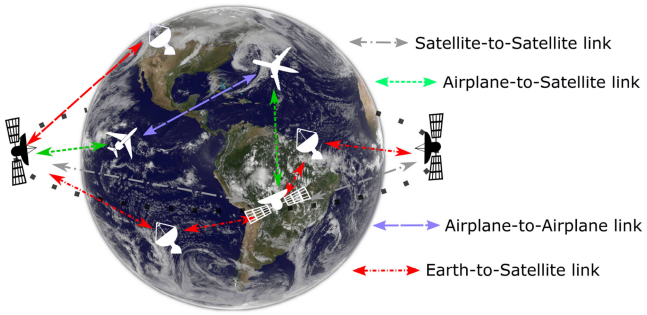

Fig. 1. An illustration of the system model considered in this paper and the several wireless links in it. Picture of Earth by NASA/NOAA's GOES Project [21].

vehicle communications, as illustrated in Fig. 1. The considered application scenarios for the channel models in this paper include: (i) airplane-to-satellite (A2S) or satellite-to-airplane (S2A), (ii) Earth-to-airplane (E2A) or airplane-to-Earth (A2E), and (iii) Earth-to-Satellite (E2S) or satellite-to-Earth (S2E). The satellite-to-satellite (S2S) case is not considered in this paper due to strong focus on modeling the molecular absorption and the atmosphere in general. Even the low Earth orbit (LEO) satellites lie in nearly empty space where any atmospheric effects will be small. Therefore, the channel mainly comprises free space loss and the antenna systems. Furthermore, although not deeply analysed, the E2S/S2E use case is equivalent to models required for possible THz band remote area communications.

The target scenario for the A2S and S2A channel modeling is shown in Fig. 2. The target scenario for channel modeling consists of an airplane at an altitude h_a and a satellite at an altitude h_s from the Earth and distance r_{as} from the airplane. The boundary of the atmosphere is r_{atm} away from the airplane. As the separation distance between the considered airplane and satellite is significant, the relative speed of the airplane is considered negligible for the channel modeling. The most important parameters and variables are given in Table I.

TABLE I
THE MOST IMPORTANT CONSTANTS, VARIABLES, AND PARAMETERS USED IN THE PAPER

Constants		
Constant	**Symbol**	**Value**
Radius of Earth	R	6,371,000 m
Speed of light	c	299,792,458 m/s
Standard pressure	p_0	101325 Pa
Standard temperature	T_0	296 K
Variables		
Variable	**Symbol**	**Unit**
Absorption coefficient	$\kappa_a(f)$	1/m
Center frequency	f_c	GHz
Parameters		
Parameter	**Symbol**	**Unit**
Altitude of airplane	h_a	m
Altitude of satellite	h_s	m
Angle to zenith	θ	rad
Depth of the atmosphere	r_{atm}	m
Distance from plane to satellite	r_{as}	m
Elevation of airplane	ϕ_a	rad
Elevation of satellite	ϕ_s	rad
Frequency	f	Hz
Pressure	p	Pa
Temperature	T	K

B. Atmospheric Propagation in the Terahertz Band

The main phenomena affecting the propagation of THz signals in the target scenarios are went through in the following. Those include free space path loss and the molecular absorption loss. Some additional loss mechanism include rain, cloud, fog, and possible scattering losses that are briefly discussed below.

1) Spreading Loss: The spreading loss measures the fraction of the power radiated by an isotropic transmitter at a frequency f that an isotropic receiver at a distance r can detect. Under the assumption of spherical propagation, the spreading loss is given by

$$\text{PL}_{\text{spr}}(f,r) = 4\pi r^2 \frac{4\pi}{(c/f)^2} = \left(\frac{4\pi f r}{c^2}\right), \tag{1}$$

where c is the speed of light in the medium, f is the frequency, and r is the distance from Tx to Rx. In our system, directional antennas (e.g., horn lens antennas, Cassegrain parabolic antennas or beamforming antenna arrays) will expectedly be utilized at the transmitter and the receiver to counter the high channel losses. In that case, their directivity gain $D(\theta,\gamma)$ with respect to an ideal isotropic emitter and detector (commonly given in dBi) needs to be accounted for.

2) Molecular Absorption Loss: The molecular absorption loss measures the fraction of electromagnetic energy that is converted into kinetic energy internal to vibrating molecules [6], [18], [22]. For an homogeneous medium with thickness r, this is given by the Beer-Lambert law and can be written as:

$$\text{PL}_{\text{abs}}(f,r) = e^{\sum_i \kappa_a^i(f) r}, \tag{2}$$

where $\kappa_a^i(f)$ is the absorption coefficient of ith absorbing species (molecule or its isotopologue) at frequency f. We denote the total summed absorption coefficient with $\kappa_a(f)$, i.e., $\kappa_a(f) \equiv \sum_i \kappa_a^i(f)$.

In our system, the medium is not homogeneous, as the density of different absorbing molecules (particularly water vapor molecules) changes drastically with altitude. In the case of vertical paths, the absorption coefficient κ_a depends on distance $\kappa_a(f,r)$ and its variations need to be accurately computed along the signal propagation path.

3) Scattering Loss on Aerosols: One possible loss mechanism comes from the aerosol scattering. The aerosols are small particles suspended by air, such as dust, ice particles, pollution, etc. Those are modelled by the Beer-Lambert law and therefore can theoretically cause significant losses over long distance links [23]. However, as it was shown in [23], the THz frequencies require rather large particles to cause significant losses. On Earth this is possible, e.g., in very dusty conditions, but in general this is not a problem at higher altitudes. The possible losses on clouds can be handled as shown below. For the sake of tractability, we ignore these losses in the further study.

4) Rain and Cloud Losses: Additional attenuation may be caused by adverse weather conditions in A2A, A2S, and S2A

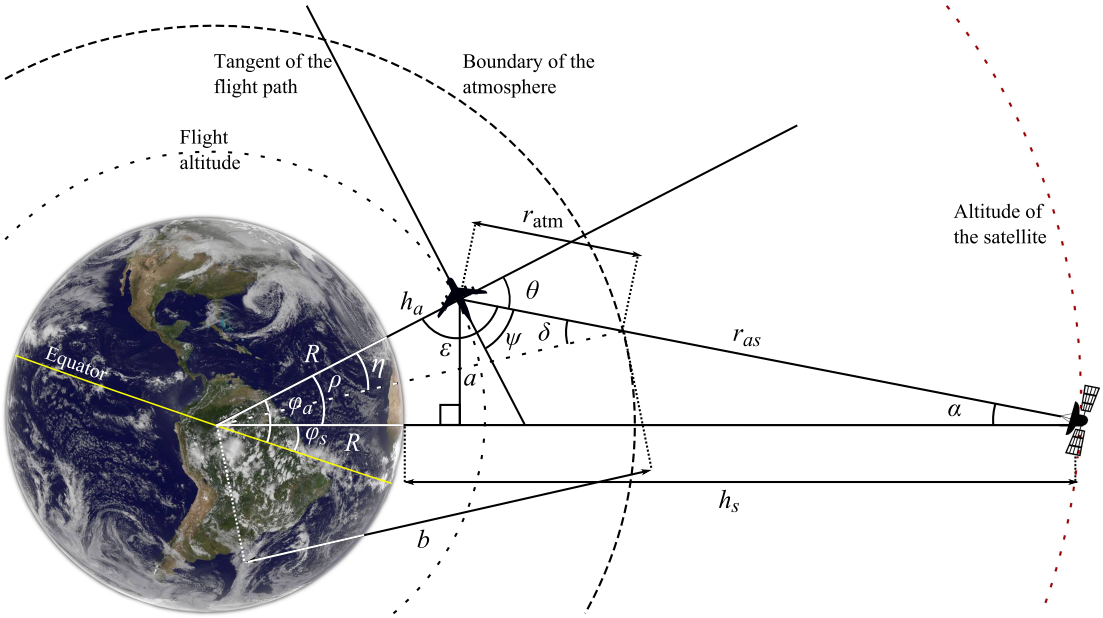

Fig. 2. The system geometry for the angles and distances in the airplane to satellite system. Picture of Earth by NASA/NOAA's GOES Project [21].

scenarios. The ITU-R provides rain [24] and cloud/fog [25] attenuation models. Those are detailed in Section III-C. It should be noted that the cloud attenuation is formally valid only up to 200 GHz frequencies [25]. Furthermore, the cloud densities, cloud thicknesses and rain rates vary greatly depending on the type of the cloud, and the probability of different types of clouds vary geographically. However, in any case the Earth to airplane or satellite paths experience added path losses ranging from few decibels up to tens of decibels in the presence of clouds and depending on the weather in general. In the further, we note the rain and cloud losses with the distance-dependant variables $\delta_{\text{Rain}}(r_r)$ and $\delta_{\text{Cloud}}(r_c)$, respectively.

III. Atmospheric Path Loss Modeling

In this section, we derive the path loss for the above aerial use cases. As highlighted in the previous section, the main challenge arises from the non-uniform molecular absorption coefficient through the atmosphere. The density, temperature, and molecular composition of the atmosphere depend on the altitude. This section gives the dynamic molecular absorption loss coefficient valid at any altitude by taking into account the impact of atmospheric parameters on the absorption line calculations. After that, we go through the transmission path geometry of slant paths through the atmosphere. Table I gives the most important constants, variables, and parameters utilized in this paper.

A. Non-Homogeneous Molecular Absorption Loss

Traditionally the channel modeling for the THz frequencies has been considered for terrestrial communications. When moving to higher altitudes, the homogeneous assumption for the line shape functions is no longer valid. We can also utilize meteorological data to take into account the global variations in water vapor content as a function of latitude, longitude, and altitude. Those will be discussed briefly in conjunction with the numerical results. Similarly, when moving to higher altitudes, mixing ratios of the molecular species change and this has to be taken into account for accurate molecular absorption modeling.

The line-by-line absorption model and the parameters required for different altitudes is presented in Appendix. Putting the absorption loss model therein together, the altitude dependent absorption coefficient becomes

$$\kappa_a^i(f, p(h_{\text{atm}}), T(h_{\text{atm}})) = \frac{p(h_{\text{atm}})\mu_i N_A}{R_g T(h_{\text{atm}})} S^i(T(h_{\text{atm}})) F^i(f, p(h_{\text{atm}}), T(h_{\text{atm}})), \quad (3)$$

where $p(h_{\text{atm}})$ is the pressure, N_A is the Avogadro constant, R_g is the gas constant, $S^i(T(h_{\text{atm}}))$ is the line intensity, $T(h_{\text{atm}})$ is the temperature, $F^i(f, p(h_{\text{atm}}), T(h_{\text{atm}}))$ is the absorption line width. The altitude h_{atm} is directly having impact on the pressure and temperature and it is indirectly affecting on the line-by-line parameters presented in Appendix depending on the altitude. The distance through the atmosphere is handled by the integration over the total molecular loss in the atmosphere and is given in the next section. The line width in the above equation is

$$F^i(f, p(h_{\text{atm}}), T(h_{\text{atm}})) = \begin{cases} F^i_{VVH}(f, p(h_{\text{atm}}), T(h_{\text{atm}})), & \text{if} \tilde{\alpha}^i_L >> \alpha^i_D, \\ F^i_D(f, T(h_{\text{atm}})), & \text{if} \tilde{\alpha}^i_L << \alpha^i_D, \\ F^i_V(f, p(h_{\text{atm}}), T(h_{\text{atm}})), & \text{if} \tilde{\alpha}^i_L \approx \alpha^i_D, \end{cases} \quad (4)$$

where $F^i_{VVH}(f, p(h_{\text{atm}}), T(h_{\text{atm}}))$, $F^i_D(f, T(h_{\text{atm}}))$, and $F^i_V(f, p(h_{\text{atm}}), T(h_{\text{atm}}))$ are the Van Vleck-Weisskopf, Doppler, and Voigt line shape functions, respectively, and α^i_L and α^i_D are Lorentz and Doppler line half widths (half width at half

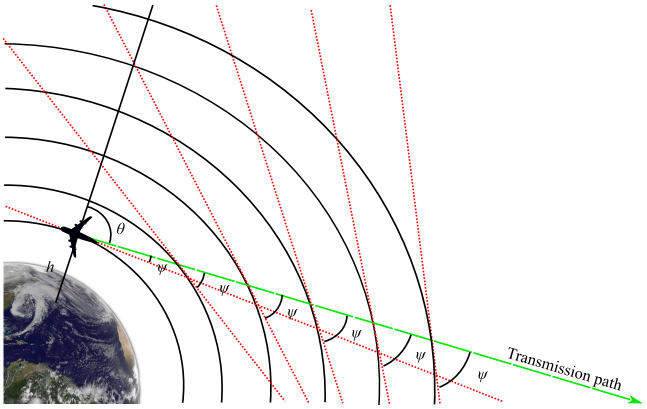

Fig. 3. System geometry on the angles of the transmission path through the atmosphere. Picture of Earth by NASA/NOAA's GOES Project [21].

maximum). The Lorentz line shapes are utilized in high pressure environment and the Doppler line shapes in low pressure environment. These are explained more deeply in the Appendix. Notice that the altitude defines the pressure, temperature, and other parameters utilized in the calculation of the absorption coefficient. As a consequence, the line shape function requires a dynamic algorithm that defines the correct line shape for every possible set of pressure, temperature, and absorption line center frequency. This can easily be done in the line-by-line algorithm by calculating and comparing the Doppler and Lorentz absorption line half-widths.

B. Transmission Path Geometry

The general system geometry is shown in Fig. 2. The usual way to model the atmosphere is to assume plane parallel atmosphere. By assuming flat surface, the geometry of the system is significantly simplified. However, when talking about applications where the entire atmosphere is penetrated, the plane parallel assumption overestimates the thickness of the atmosphere. The impact is the higher the lower is the angle to the surface. In order to rectify the problems with the plane parallel model, in this work we model realistic curving atmosphere. In such setting, the problem becomes with ever-changing angle to the zenith (and to the elevation angle ψ) as shown in Fig. 3. This problem can be modeled geometrically by utilizing the geometry shown in Fig. 2. In this figure, R is the Earth's radius, h_a is the altitude of the airplane, b is the Earth's radius plus the total thickness of the atmosphere, h_s is the altitude of the satellite, ϕ_a is the elevation of the airplane, ϕ_s is the elevation of the satellite, r_{as} is the distance from the airplane to satellite, and r_{atm} is the most interesting parameter, i.e., the distance through the atmosphere from the airplane to the boundary of the atmosphere. This latter distance is important because of the molecular absorption that depends on the altitude and the constantly evolving line parameters as the altitude changes. It should be noted that the elevation herein means an arbitrary angle that is used to define the geometry between the Earth, airplane, and the satellite. Herein, it is bound to the latitude to illustrate the angles easily. However, in the case of moving airplanes, the angular differences have to be bound to both latitude and longitude based on the real locations of the network elements.

The main difference of the curving atmosphere to the plane parallel atmosphere comes from the dynamically changing atmospheric parameters depending on the altitude. This is shown in Fig. 3. Distance from the airplane to satellite is given by the law of cosines

$$r_{as} = \sqrt{(R+h_a)^2 + (R+h_s)^2 - 2(R+h_a)(R+h_s)\cos(\rho)}, \tag{5}$$

where R is the radius of Earth, h_a is the altitude of the airplane, h_s is the altitude of the satellite, and ρ is the angle between the airplane and satellite looked from the center of the Earth. This angle is obtained as subtraction of the elevation angles, i.e., $\rho = |\phi_a - \phi_s|$, where ϕ_a is the elevation of the airplane and ϕ_s is the same for the satellite. See details on these variables in Fig. 2. The distance from airplane to imaginary line from Earth's core to satellite is calculated as

$$a = (R+h_a)\sin(\rho). \tag{6}$$

Then the angle between the satellite and the airplane, looked from the satellite, is obtained from the two as

$$\alpha = \sin^{-1}\left(\frac{a}{r_{as}}\right). \tag{7}$$

The angle between line from Earth to airplane and the line from airplane to satellite is give simply by

$$\epsilon = 180^\circ - \alpha - \rho, \tag{8}$$

which is also equivalent to $\epsilon = \psi + 90^\circ$ where ψ is the elevation angle of transmissions path from airplane to satellite. These angles also directly give the transmission angle with respect to zenth as $\theta = 180^\circ - \epsilon = 90^\circ - \psi$. Now we have everything we need in order to calculate the distance from airplane through the atmosphere r_{atm}. This can be calculated from the triangle suspended by $R + h_a$, distance from the core of the Earth to boundary of the atmosphere b, and r_{atm}. Let us first calculate the corner angles of this triangle. We can obtain angle δ from law of sines

$$\delta = \sin^{-1}\left(\frac{(R+h_a)\cos(\epsilon)}{b}\right). \tag{9}$$

Then we can obtain last angle as $\eta = 180^\circ - \epsilon - \delta$. Finally we can obtain the distance through the atmosphere r_{atm} with the law sines as

$$r_{\text{atm}} = \frac{b\sin(\eta)}{\sin(\epsilon)}. \tag{10}$$

On the other hand, we could also solve r_{atm} with the law of cosines and the quadratic formula as

$$r_{\text{atm}} = (R+h_a)\cos(\epsilon) + \frac{1}{2}\sqrt{(-2(R+h_a)\cos(\epsilon))^2 - 4((R+h_a)^2 - b^2)}. \tag{11}$$

Both of these expressions for r_{atm} are equal, but the former gives perhaps a bit more compact way to calculate the angles and the

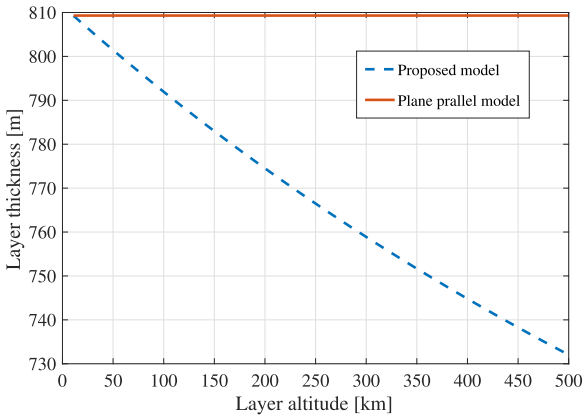

Fig. 4. Comparison of the layer thickness of the plane parallel atmosphere and a round atmosphere as a function of altitude.

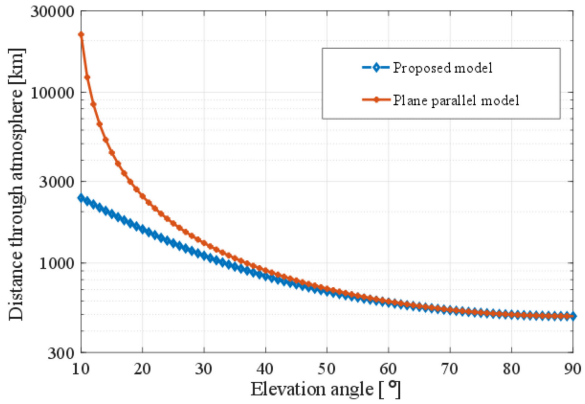

Fig. 5. A comparison of the total distance through the atmosphere according to the plane parallel assumption and the model herein as a function of the elevation angle.

distances. Finally, in order to fit this new approximation for the length of the atmosphere to the transmittance, we need to take a derivative of it. The reason is that the absorption coefficient changes as a function of the altitude, but does not depend on the total distance. Therefore, we need to manipulate the space over which the total absorption is calculated. That is, we multiply the absorption coefficient by $d/dr(r_{\text{atm}})$ instead of $\sec(\theta)$ as in the case of plane parallel atmosphere. Then,

$$\tau(f,r) = e^{-\int_{r_1}^{r_2} \kappa_a(f,r)\frac{d}{dr}r_{\text{atm}}dr} = e^{-\int_{r_1}^{r_2} \kappa_a(f,r_{\text{atm}})dr_{\text{atm}}}. \quad (12)$$

The difference between the plane parallel assumption and the proposed model is shown in Figs. 4 and 5. In computer simulations/models, we are forced to discretize the parameters due to utilization of the data bases to obtain the parameters and since the computer inherently handles only discrete data. Then we also have to discretize the atmosphere into equally spaced layers. In the plane parallel atmosphere, the distance through each layer is same at all altitudes due to the simple geometry. In the geometry given above, the discretization leads into non-equal propagation distance through the layer depending on the altitude and the angle of penetration due to curvature of the atmosphere. It can be seen in Figs. 4 and 5 that the vertical path through the atmosphere is exactly the same for both model as they should be. Notice that the atmosphere has been calculated up to 500 km altitude where it is already very thin and does not contribute much on the propagation anymore. Fig. 4 shows the propagation distance through a single 500 m layer (500 m resolution accuracy) at 38.2° angle from the ground. As stated above, the layer altitude has impact on the dynamic distance through the atmosphere. Thus, the plane parallel assumption tends over estimate the layer thickness. The problem is the worse the lower is the angle through the atmosphere. This is well visible in Fig. 5, which shows the total distance through the atmosphere. As the molecular absorption is dependent on the propagation through molecular medium, the plane parallel assumption may greatly overestimate the total absorption loss. The next section looks into derivation of the absorption coefficient $\kappa_a(f,r)$ as the geometry of the propagation is one important issue, and the second important aspect are the parameters fed into the model.

C. Total Path Loss

By combining (1) with (12), the total path loss can be written as

$$\text{PL}(f,r) = \frac{(4\pi r_{as} f)^2 \delta_{\text{Rain}}(r_r)\delta_{\text{Cloud}}(r_c)}{c^2 G_{\text{Tx}}(\theta_{\text{Tx}})G_{\text{Rx}}(\theta_{\text{Rx}})} e^{\int_{r_1}^{r_2} \kappa_a(f,r_{\text{atm}})dr_{\text{atm}}}, \quad (13)$$

where $G_{\text{Tx}}(\theta_{\text{Tx}})$ and $G_{\text{Rx}}(\theta_{\text{Rx}})$ are the Tx and Rx antenna gains towards directions θ_{Tx} and θ_{Rx}, respectively, and $\delta_{\text{Rain}}(r_r)$ and $\delta_{\text{Cloud}}(r_c)$ are the channel gains due to rain and cloud losses, where r_r is the distance through the rain and r_c is the distance through the cloud/fog.

The rain loss is given by [24]

$$\delta_{\text{Rain,dB}}(r_r) = kR_r^{\alpha} r_{\text{eff}}, \quad (14)$$

where k and α are parameters tabulated in [24], R_r is rain rate (mm/hr), and r_{eff} is the effective distance that is a multiplication between the actual distance r_r and a distance scaling factor. This scaling factor is detailed in [26, Sec. 2.4.1]. The cloud loss is given by [25]

$$\delta_{\text{Cloud,dB}}(r_c) = K_l M r_c, \quad (15)$$

where K_l is the specific attenuation coefficient and M is the liquid water density (g/m^3) in cloud or fog. It should be noticed that the above losses are specified in the ITU-R recommendations in decibel scale (hence the dB-subscript in the above equations). More details on the parameters for these models can be found in [24] and [25].

IV. Received Signal Power

In order to calculate the SNR and subsequently the channel capacity of the links under study, this section studies the properties of the received signal including the noise.

A. Total Received Signal Power

The received signal power spectral density Y at the receiver is given by

$$Y(f,r) = X(f)\text{PL}(f,r) + N(f,r), \tag{16}$$

where $X(f)$ is the transmitted signal power spectral density with total power $P_{\text{Tx}} = \int_W X(f)df$ and W is the signal bandwidth, $\text{PL}(f,r)$ is the total path loss given by (13), and $N(f,r)$ refers to the total noise power spectral density. As we discuss next, the calculation of the noise at THz frequencies is a non-trivial process.

B. Noise

The last piece of the puzzle before calculating the SNR is the noise. The noise is an interesting problem in THz band since the molecular absorption process introduces additional antenna noise due to atmosphere acting as black body radiator, i.e., the atmosphere emits radiation according to the Planck's law. At regular atmospheric temperatures, the atmospheric black body radiation begins to contribute significantly around sub-THz frequencies. This can be modelled via antenna brightness temperature. There are two options: at lower frequencies, where $hf \ll k_B T$, the Rayleigh-Jeans law can be utilized [27]. At higher frequencies, this model suffers from so called ultraviolet catastrophe, i.e., it gives infinite overall black body energy due to ever-increasing energy as a function of frequency. The second option is to use Planck's law, which is accurate everywhere, and is given as [27]

$$B_f(f,T) = \frac{2hf^3}{c^2(e^{\frac{hf}{k_B T}} - 1)}. \tag{17}$$

Then the brightness temperature becomes

$$T_b = \frac{hf}{k_B}\ln\left(1 + \frac{e^{\frac{hf}{k_B T(d)}} - 1}{1 - \exp(-\int_{r_1}^{r_2}\kappa_a(f, r_{\text{atm}}, p, T)dr_{\text{atm}})}\right)^{-1}, \tag{18}$$

where T is the average temperature, or temperature profile of the atmosphere and the last term comes from the derived channel model and $1 - \exp(-\int_{r_1}^{r_2}\kappa_a(f, r_{\text{atm}}, p, T)dr_{\text{atm}})$ gives the emissivity of the atmosphere. Though the Raleigh-Jeans law can be used in the low THz band, our model used the more accurate Planck's law to determine the brightness temperature of the atmosphere.

Besides the atmospheric noise, the thermal noise at the receiver needs to be taken into account. The thermal noise begins to decrease at the THz frequencies due to quantum effects at very low temperatures, or very high frequencies, i.e., when $hf \gg k_b T$. At this region, the probabilities of the higher energy states of the molecules/atoms become smaller and smaller, making the thermal noise smaller and smaller with respect to the one predicted by simple $k_B T$ [28]. Taking into account the total noise power degradation, the thermal noise power density with receiver noise figure N_f (in dB) becomes

$$\begin{aligned} N_T(f, N_f) &= k_B T\eta(f)10^{N_f/10} \\ &= k_B T\frac{hf/k_B T}{\exp(hv/k_B T) - 1}10^{N_f/10} \\ &= \frac{hf}{\exp(hv/k_B T) - 1}10^{N_f/10}, \end{aligned} \tag{19}$$

where function $\eta(f)$ takes into account the noise power reduction. However, $\eta(f)$ does not play crucial role in the THz communications, since the transition when quantum of energy exceeds per Hertz thermal noise power occurs at 6.168 THz at 296 K temperature, i.e., when $k_B T = hv$. Therefore, the noise reduction is modest, up to few dBs at 10 THz frequency. Considering the fact that the THz band systems are envisioned to be extremely wide band systems, there is far more noise than in the conventional systems, mainly contributed by the large thermal energy of the wide band systems.

Finally, the total noise power spectral density at the receiver becomes:

$$N(f) = B_f(f,T) + N_T(f, N_f). \tag{20}$$

The total noise power can be then obtained by integrating N over the receiver bandwidth, W in our model.

C. The System SNR and Capacity

Taking into account the noise and the path loss from above, the SNR becomes

$$\text{SNR}(f,r) = \frac{X(f)\text{PL}(f,r)}{N(f)}, \tag{21}$$

and the corresponding Shannon capacity is

$$C(r) = \int_W \log_2(1 + \text{SNR}(f,r))df. \tag{22}$$

V. Numerical Results

In this section, we evaluate the expected path losses and link performances based on the above channel models.

A. Parameters for the Channel Model

One important factor in modeling the atmosphere is to model the altitude dependent parameters correctly. Those are mainly the temperature and pressure, and volume mixing ratios of different molecules. All these vary quite a bit as a function of altitude. For this work, we utilized the 1976 US Standard Atmosphere [29]. The corresponding temperature and pressure as a function altitude is given in Fig. 6. The volume mixing ratios of common molecules is given in Fig. 7. Interestingly, the volume mixing ratios of the molecules remain roughly the same to the sea level up until 86 km altitude, after which they start to vary to each other. The pressure, temperature, volume mixing ratios, and ground level humidities are shown in Figs. 6 to 8.

If one is interested modeling applications close to ground level, the global average humidities and the ground height has an impact on the molecular absorption loss. This mostly depends on the elevation angle, but also in the exact location in some cases. Fig. 8 shows the average humidity around the world (left) and the ground height (right). The data for these were obtained

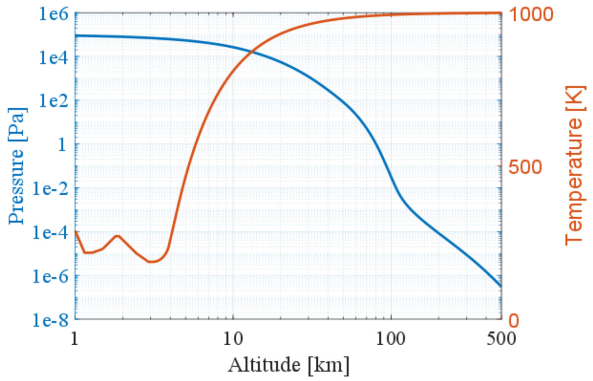

Fig. 6. Atmospheric pressure and temperature as a function of altitude.

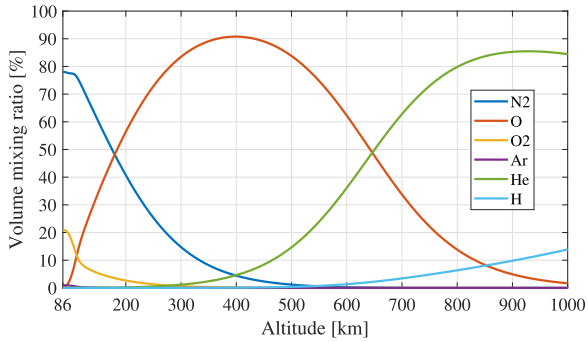

Fig. 7. Volume mixing ratios of different molecules as a function of altitude.

from NASA/GMAO MERRA2 reanalysis data [30]. From [30], one can find large datasets of atmospheric data, including global humidity data at different time scales and much more related to global weather and climate.

The rain and fog attenuations were shortly discussed above. In the real atmosphere, we do not always have clear weather and additional losses by clouds and rain impair the link performance. These are the mostly affecting low altitude communications, below few kilometer heights. As such, they have small impact on A2S and communications while at the typical flight heights. However, some losses by clouds can also exist at very high altitudes. For the take off and landing phases these may have an impact, and also in the G2A use case.

In the below example shown in Fig. 9, we assume a typical nimbostratus cloud, which is roughly one kilometer thick and has a cloud bottom height of 0.7 km [31]. The cloud density is assumed to be 0.5 g/m^3, which is close to a typical density of a nimbostratus cloud [31]. The rain rate is assumed to be 5 mm/hr, which corresponds to a moderate rain. Figure 9 shows the impact of the clouds and rain with the above assumptions for a slant path and path angled at 45 degrees. The angled path therefore increases the path lengths inside the rain and clouds by $\sec(\theta = 45^\circ)$, or $\sqrt{2}$. We can see that the losses vary from few decibels to few tens of decibels. Depending on the frequency and other losses, this may cause problems in signal reception and should be taken into account in the link budget considerations. However, as mentioned above, the rain and cloud/fog attenuations are mostly affecting low altitude communications, such as E2A communication scenario.

TABLE II
THE SIMULATION PARAMETERS USED IN THE NUMERICAL RESULTS

Parameter	Symbol	Value
Transmit power	P_{Tx}	1 W
Transmission bandwidth	W	5 GHz
Noise figure	N_f	10 dB
Antenna diameter at airplane	d_A	0.5 m
Antenna diameter at satellite	d_A	1.0 m
Aperture efficiency	A_e	70%
Elevation difference	ρ	0–12.5°
GEO orbit	h_s	35,786 km
LEO orbit	h_s	500 km
Ground level temperature	T	288.15 K
Ground level pressure	p	101325 Pa

The simulation parameters for the rest of the numerical results are given in Table II unless otherwise stated. The antenna gains are calculated with a parabolic antenna equation

$$G(f) = A_e \left(\frac{\pi d_A}{\lambda} \right)^2, \tag{23}$$

where A_e is the aperture efficiency, and d_A is the diameter of the antenna. We can see that the antenna gain increases to square of frequency for fixed size dish when increasing the frequency. Adding dishes at both ends of the link, the ideal gain of the antenna gain can be very large and even overcome the electric size of the antenna visible in free space path loss equation $(\lambda^2/4\pi)$. In the low absorption loss region, for fixed distance, the SNR can therefore theoretically get better when increasing the frequency. This is also shown later in the SNR calculations.

The parabolic antennas have advantage of providing a lot gain in relatively compact package than can be mounted on fuselage of the airplane. Such antennas require an aerodynamic cover to protect the antenna and to interfere as little as possible with the overall aerodynamics of the airplane. The downside is the need for physical beaforming that limits visibility of all the paths and restricts the maximum beamforming angles to at most the horizon with respect to the antenna mount, but most likely less to keep the antenna profile low. If there is a downward link, a separate antenna is required at the bottom of the fuselage.

The transmission power was chosen to be modestly low to take into account the fact that at the moment generating a lot of power in the THz band is difficult. The bandwidth is chosen to be rather low to decrease the noise bandwidth, which is very important design aspect for the prospective long range THz communications. What is the large enough bandwidth that justifies the THz band, but keeps the noise floor small enough. The antennas are typical parabolic antennas with 70% aperture efficiency. To show the impact of the angular differences between the satellite and the airplane, we utilize 0°, 6.25°, and 12.5° elevation differences between the two. At GEO orbit being at 35 786 km height and LEO orbit at 500 km height, those correspond to 0–14.7° angle (14.7° at 0–20 km altitude for 12.5° elevation difference) from the zenith at airplane to GEO satellite and 0–78° degree angle for the LEO orbits (58.5–77.2° zenith angle at ground level and 59.6–78.0° at 20 km altitude). These correspond to angles from the horizon of the airplane to satellite varying from 12-90°. These elevation differences correspond to link distances in S2A to vary

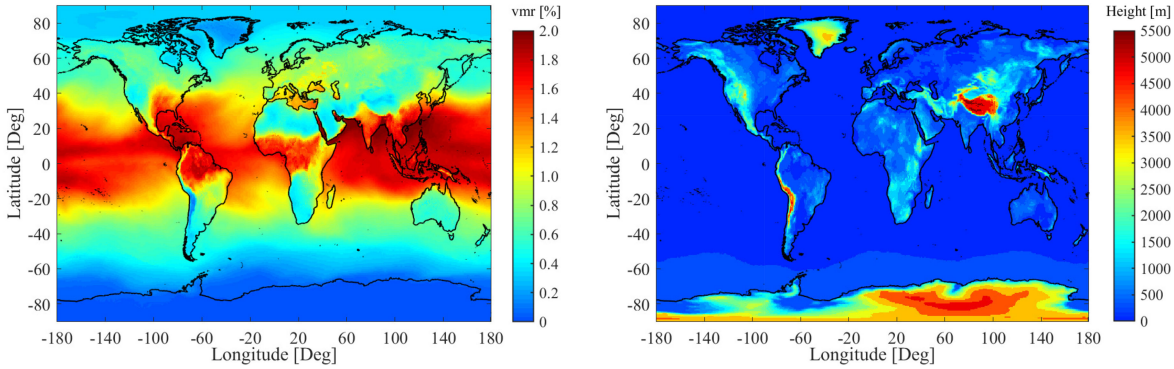

Fig. 8. The surface volume mixing ratio of water vapor (left) and the surface height from the sea level (right).

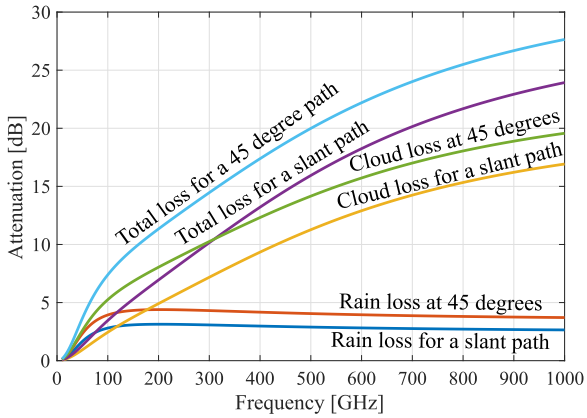

Fig. 9. Rain and cloud attenuations for slant paths as well as for 45° angled paths from zenith.

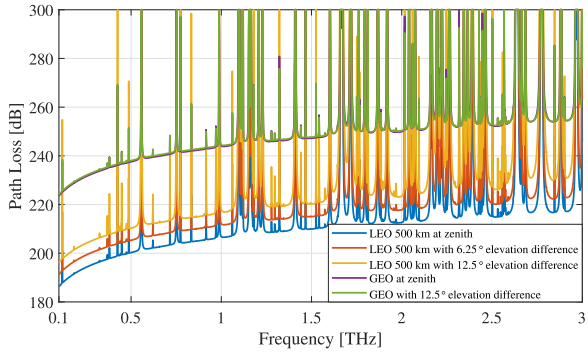

Fig. 10. Path loss from airplane to satellite for LEO and GEO orbits as a function of frequency. The airplane altitude is 11 km.

from about 500 to 1526 km for the LEO orbit at 500 km altitude depending on the airplane altitude (that is rather small compared to the total link distance), and 35 786 – 35 964 km for the GEO orbit.

B. Path Losses

Figure 10 shows the path loss from airplane to satellite for an airplane at 11 km altitude as a function of frequency. The path losses are shown for a geostationary Earth orbit (GEO, ∼36 000 km) and for a low Earth orbit (LEO) at 500 km altitude. The path losses have been calculated for zenith path and for elevation differences 6.25–12.5° through the atmosphere for the LEO orbit, and 12.5° elevation difference for the GEO due to smaller differences between the path losses between different angles. The LEO connection suffers more from the angled paths due to the path loss by absorption has more relatively higher impact on the shorter paths. The GEO path loss is dominated by the FSPL and the absorption does not have a that large impact on the total path loss. We can see that the path losses are considerable. Those range from about 190 to 260 dBs disregarding the absorption peaks that are much higher. This means that the required antenna gains need to be very high, but at the same time, the bandwidths need to be low enough to keep the noise level down and to avoid the absorption peaks. Considering fixed aperture antennas, the antenna diameters need to be in the order of 0.5–1 meters to provide enough gain in the ideal case. Furthermore, LEO path loss towards zenith as a function of distance and frequency is given in Fig. 11. This figure shows that the FSPL dominates vast majority of the high altitude links with molecular absorption loss increasing towards the high frequencies and the lower altitudes. This implies that the A2S/S2A links provide the best performance at the higher flight altitudes as it will be shown later.

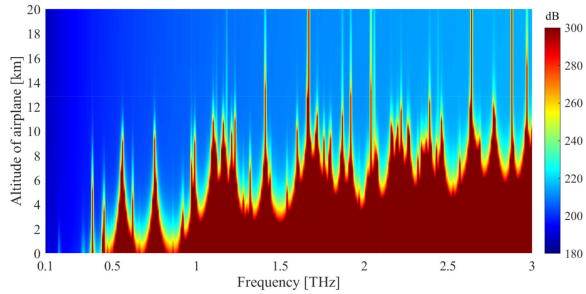

Fig. 11. Path loss from airplane to satellite for 500 km LEO satellite as a function of frequency and airplane altitude.

The path losses from Earth to airplane as a function of airplane altitude are shown in Figs. 12 and 13 for a frequency range from 100 GHz to 1000 GHz. The latter figure assumes LEO height of 500 km. Any frequencies above 1000 GHz are effectively

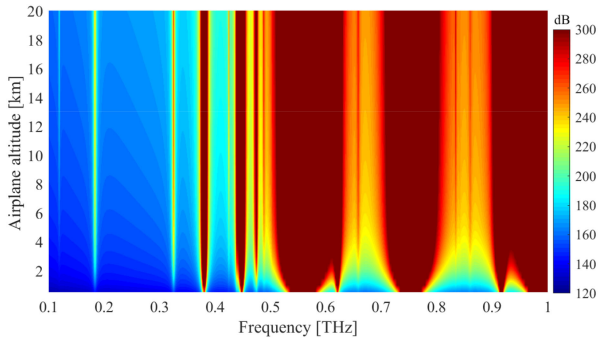

Fig. 12. Path loss from Earth to airplane as a function of airplane altitude and frequency.

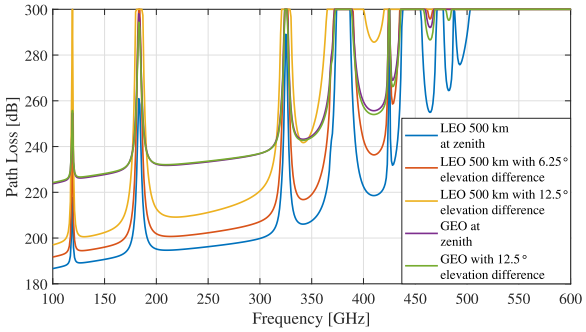

Fig. 13. Path loss from Earth to satellite as a function of frequency.

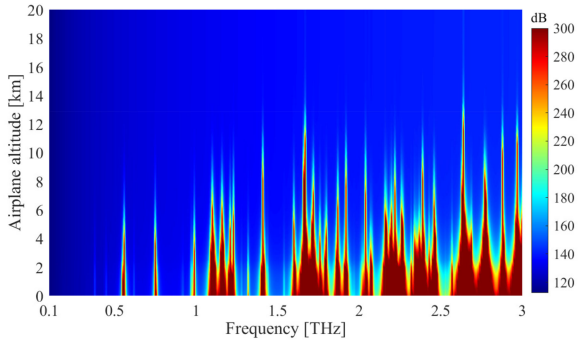

Fig. 14. Path loss from airplane to airplane (common altitude) for a 100 m link as a function of airplane altitude and frequency.

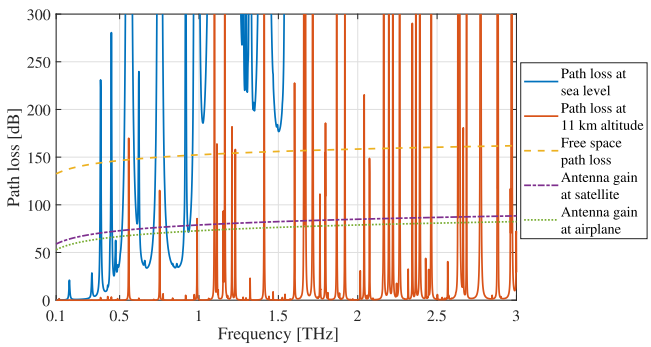

Fig. 15. Comparison of path losses per kilometer for FSPL, molecular absorption loss at sea level and 11 km altitude, and antenna gains of 0.5 and 1 m ideal dish antennas.

blocked due to high absorption loss close to Earth. We can see that the below 380–450 GHz frequencies are utilizable for airplane communications from the ground. However, the losses remain high and partially so due to high FSPL at high frequencies. This also means a certain type of a bottle neck for feeding the satellites. The airplane to satellite links suffer less from the atmospheric loss and could theoretically utilize higher frequencies that than the Earth to airplane, or Earth to satellite links. This potentially opens a door for frequency division between ground to satellite and air to satellite links. However, this is also dependent on the capacity requirements, and hardware limitations. The latter is a major problem at the THz frequencies and potentially considerable losses have to be expected from inefficiency of them. In this paper we do not consider those, as the development of the THz band hardware is still a major research topic and relatively poorly understood from the viewpoint of realistic system and link performance. It should still be kept in mind that more losses are expected compared to pure atmospheric losses due to rain, clouds/fog, and other possible mechanism, such as the scattering loss.

Airplane to airplane path loss for a 100 m link is shown in Fig. 14 as a function of altitude and frequency. As expected, the path loss decreases with altitude and makes the communications more simple. Above 10 km height, the loss is mostly comprised of the FSPL disregarding some spikes in the spectrum. This is also shown in Fig. 15, which shows the path losses per kilometer link on ground level and at 11 km height. As a reference, the antenna gains for 0.5 m diameter dish antenna ('airplane antenna') and 1 m diameter dish antenna ('satellite antenna') are also shown. It should be noticed that the airplanes in general fly far away from each other and 100 m distance would be considered very dangerous. The airplane to airplane links do not have many use cases in civil aircrafts, but would be potential for military applications and in drone-to-drone applications. Also, these figures are applicable to on Earth communications due to varying land height. On a general note on the high frequency links, the THz band offers a natural protection against third parties to listen to the data traffic as the FSPL and atmospheric losses kill the signals over long distances in the lower atmosphere as seen in Fig. 12 and 14.

C. SNR and Capacity

Based on the path losses, we can estimate the performance of the extremely long links. Figure 16 shows the path losses from A2G and S2A (or G2A and A2S) as a function of the airplane altitude for 660 GHz and 940 GHz center frequencies. The satellite is on LEO orbit at 500 km height and we show results also for 12.5° elevation difference. As it can be expected, there is a crossover altitude for the lower loss connection direction. This crossover point depends on the frequency and the elevations of the airplane and the satellite, but suggests that the best way to provide THz connectivity would be to have both links available. During the mid-flight, the satellite link provides better connectivity. Considering that the use of electronic devices

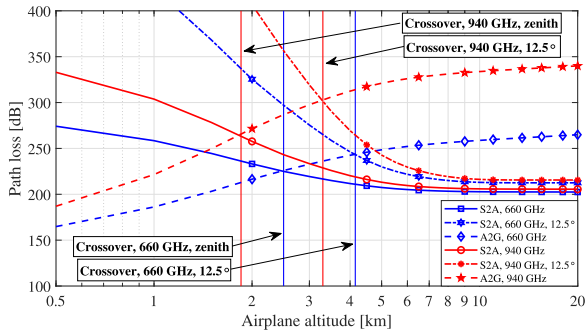

Fig. 16. Comparison of A2G and A2S path losses at 660 and 940 GHz center frequencies as a function of the airplane altitude for zenith paths and inclined paths with crossover altitudes where of the minimum loss path.

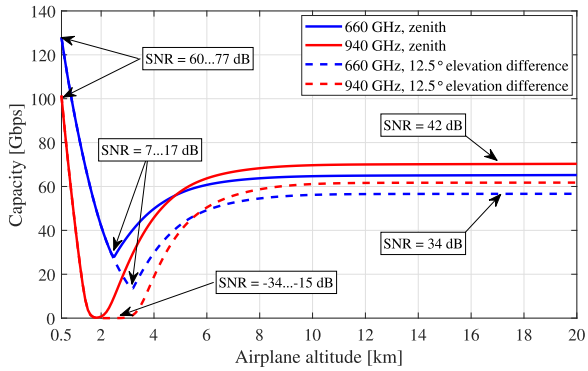

Fig. 17. Comparison of A2G and A2S capacities at 660 and 940 GHz center frequencies as a function of the airplane altitude for zenith paths and inclined paths. The shown capacity is for the minimum path loss path from Fig. 16.

is not allowed during the take off and landing, the satellite link alone would be enough for the passenger use. These crossover altitudes are approximately 1.85 km (at $\rho = 0°$) and 3.3 km (at $\rho = 12.5°$) for 940 GHz frequency and 2.5 km (at $\rho = 0°$) and 4.15 km (at $\rho = 12.5°$) for 660 GHz. It should also be noticed that the calculation herein does not take into account the movement of the airplane that would have more severe impact towards ground since the link distance is much lower that towards the satellites. The true path loss towards the ground would therefore also depend on the available ground stations and their locations, which would increase the distance and the path loss, most likely very significantly rendering the low altitude communications challenging. Especially with physical beam steering that is not as agile for handovers as electronic beamsteering techniques.

Figure 17 provides the capacity figures for the calculated minimum path losses in Fig. 16 assuming 1 W transmit power, 5GHz bandwidth, 10 dB noise figure, and 0.5 m dish antenna at airplane and 1 m dish antenna at satellite and ground. With these figures, The link budget is formed of the 30 dBm transmit power, -67 dBm noise floor, uplink antenna gains of 69.2 dBi 72.3 dBi for 660 GHz and 940 GHz frequencies, respectively, and downlink gains of 75.2 dBi and 78.3 dBi for 660 GHz and 940 GHz frequencies, respectively. Combined with the path losses in Fig. 16, the resultant SNR figures on some specific points are given in Fig. 17. The capacities can exceed 150 Gbps at close proximity to Earth station. Mid-flight capacities ranging from 55–70 Gbps can be achieved. Interestingly, whereas the 940 GHz band performs worse close to Earth, it gives increased capacity at higher frequencies compared to 660 GHz band. This is attributed to the higher antenna gains at higher frequencies. This is an interesting results that shows good potential of very high frequencies for A2S scenarios even if usability of close to 1 THz frequencies and beyond are difficult on surface level due to very high path loss. The capacity and SNR figures herein are remarkably good considering the high path losses. Theoretically, the calculated SNRs would be able to support very high modulation orders. In the reality though, additional losses should be expected and combined with possible adverse weather conditions, the real average SNRs would be lower. However, these are very promising figures for the future ultra-high distance THz communications.

The expected SNR as a function of altitude and frequency for A2S link to GEO orbit is given in Fig. 18. As a consequence of the fixed apertures, the effective antenna gain increases to the square of the frequency per antenna. This is seen as one of the potential source to compensate the high losses in the channel; It will be easier to make electrically large antennas at THz frequencies that significantly increase the antenna gains [32]. As the antenna gains at both ends of the link increase to square of the frequency according to (23), this translates into increasing SNR as a function frequency in Fig. 18 as the free space path loss increases to the square of frequency. The SNR is further increased by the altitude of the plane due to before mentioned lower absorption loss at high altitudes. In the real world, the antenna losses and power generation become more difficult when moving to higher frequencies. This can be expected to decrease the overall transmission performance at higher frequencies. However, the ideal results herein have shown great potential with room to move even with higher expected losses. Figure 18 also shows the SNR limits of some modulation methods for 10^{-6} target BEP values for 1 GHz bandwidth signal. Namely, for 16-QAM and BPSK. As expected of the long distance links in the THz band, the usable modulation orders remain modest to ensure good BEP performance. It should be noted that the BER values are pure physical layer BEPs and do not take into account coding. Thus, the actual BERs would be better with lower overall throughput due to coding overhead.

Whereas the overall picture favor the higher frequencies because of theoretically higher achievable antenna gains, the reality is that the hardware imperfections would most likely decrease the performances as the frequency is increased. However, the results herein show great potential for the THz frequency band for long distance communications. There are many obstacles ahead to realize these types of systems. Most notably in the hardware side, but with time and leaps the THz communications has taken during the past few years, these frequencies will truly be conquered in the near future. This also then opens doors for wide range of multiple scales of communications on these frequencies. As an example, to provide high speed satellite communications for the airplanes.

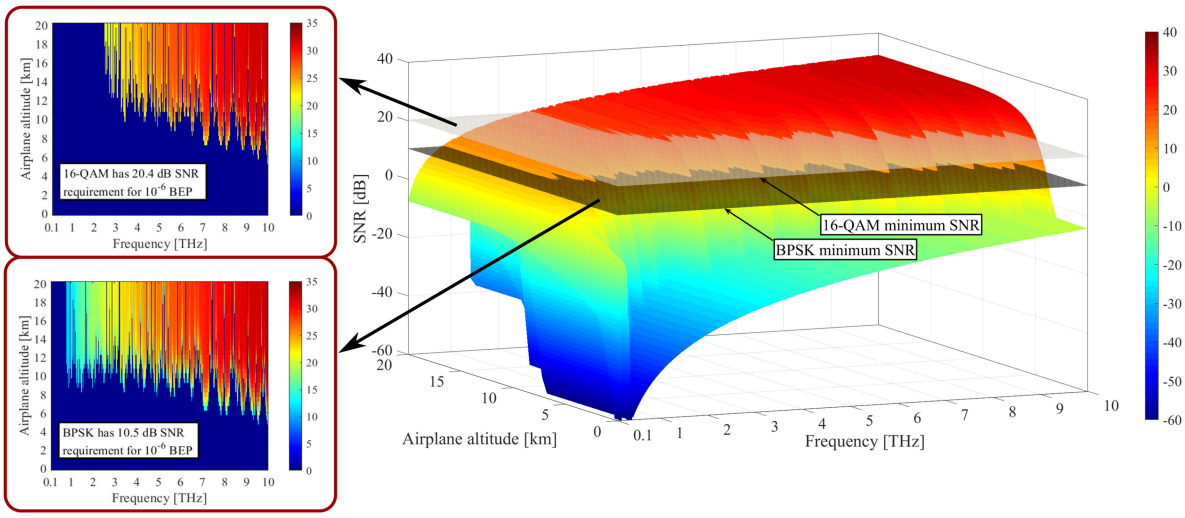

Fig. 18. SNR from satellite to airplane as a function of airplane altitude and frequency for GEO orbit. Figure also shows boundaries for square gray coded 16-QAM and BPSK for target BEP probability of 10^{-6}.

VI. Conclusion

We presented a channel model for airplane communications in the THz band in this paper. The results show that the path losses in airborne links are very high, as it can be expected from an extremely high distance links operating at very lossy THz frequencies. However, if the antenna apertures are high, potentially very large antenna gains can be achieved. Regardless of the very high path loss, airplane to satellite, and airplane to airplane communications are perfectly possible on rather wide spectrum. The Earth to satellite or airplane case is more demanding due to high absorption loss close to Earth. This may limit the Earth communications to below 380 GHz frequencies. In practice, the 100–300 GHz frequency bands are in any case the first frequencies to be commercially utilized in the near future. Possible weather impacts will decrease the signal levels, and increasingly so at higher end of the THz band. The frequency regulation, on the other hand, will limit the full utilization of the THz frequencies in the space applications due to protection of the passive Earth observation services. Although it is often said that the THz frequencies are only for short distance communications, they also have great potential in long distance applications. This is especially the case in space where the atmosphere causes less channel losses. The numerical results herein showed that the THz band is a very promising platform for high capacity links, especially when the applied in high atmosphere. The main outcome of this paper were the LOS channel model for high distance THz communication links and a feasibility analysis of the THz band for those. The future work will leverage the results by studying real flight paths in simulation models with cloud coverage and global weather. Based on the results in this paper, the real flight paths will offer very good performance during the mid-flight at high altitudes. The take-off and landing are the most challenging parts of the flight to provide feasible capacity, but on the other hand those are the times when electronic devices need to be in offline mode. Therefore, the future of high frequency communications to bring maximum capacity for the airplanes looks really bright.

Appendix

We give the derivation of the molecular absorption coefficient in different atmospheric conditions below. The absorption loss was described Section II-B and it depends on the link distance and absorption coefficient. The latter depends on pressure, temperature and molecular composition as

$$\kappa_a^i(f) = N_i \sigma_i(f), \tag{24}$$

where N_i is the number density and $\sigma_i(f)$ is the absorption cross section of the ith absorbing species. The number density N_i for the absorbing species i can be estimated by the ideal gas law [6], [18]

$$N_i = \frac{p}{p_0}\frac{T_0}{T}\mu_i n_0 = \frac{p}{p_0}\frac{T_0}{T}\frac{p_0}{R_g T_0}\mu_i N_A = \frac{p}{R_g T}\mu_i N_A, \tag{25}$$

where p_0 and T_0 are the standard pressure and temperature (101 325 Pa and 296 K, respectively), p is the pressure, T is the temperature, μ_i is the volume mixing ratio of absorbing species i, R_g is gas constant ($R_g = k_B N_A$), k_B is the Boltzmann constant, N_A is the Avogadro constant and $n_0 = p_0 N_A/(R_g T_0)$ the number density of the molecules in standard pressure and temperature.

Different molecules have specific abundances in atmosphere. In addition, the different isotopologues of the molecules have their natural abundances [6], [18]. We have included all the abundances of molecules and their subspecies into the variable μ_i. The abundances of atmospheric molecules and the other parameters for line-by-line calculations can be found in high-resolution transmission molecular absorption database (HITRAN) [33]. Other similar models to HITRAN, such as GEISA [34] and JPL [35], also exist.

The absorption cross section $\sigma_i(f)$ is calculated as a product of spectral line intensity $S^i(T)$ and spectral line shape $F^i(p,f,T)$ ($\sigma_i(f) = S^i(T)F^i(p,f,T)$). The absorption cross section gives the effective absorption area for a single particle. The spectral line intensity gives the absorption strength of the spectral lines and spectral line shape gives the shape of the absorption lines. The line shape is normalized so that the integration over the line shape equals unity [36]. It should be noticed that line intensity depends only on temperature and line shape depends on frequency, pressure and temperature. For simplicity, we will use notation $F^i(f)$ for line shape, as the line shape is calculated for each line center f_0^i. In order to calculate the line shape $F^i(f)$, the resonance frequencies f_c^i of the line centers f_0^i must be calculated first. The resonance frequencies increase from zero-pressure position f_0^i according to [6], [22]

$$f_c^i = f_0^i + \delta_i \frac{p}{p_0}, \tag{26}$$

where δ_i is the linear pressure shift.

Even though the absorption process is discrete in frequency domain, the individual absorption lines are spread due to collisions between the molecules (Lorentz broadening), as well as because of the velocity of the molecules (Doppler broadening). The pressure broadening can be expressed with Lorentz half-width α_L^i (at pressures higher than 10 kPa [22]). This can be obtained from foreign and self-broadened half-widths α_0^f and α_0^i respectively by [18], [22]

$$\alpha_L^i = [(1-\mu_i)\alpha_0^f + \mu_i \alpha_0^i] \left(\frac{p}{p_0}\right) \left(\frac{T_0}{T}\right)^{\gamma}, \tag{27}$$

where γ is temperature broadening coefficient. Self-broadening is caused by the collisions between molecules of the same species, while foreign-broadening is due to the inter-molecular collisions. The coefficients γ, α_0^f and α_0^i can be obtained from the line catalogues.

At high air pressure, Lorentzian line shapes are utilized [37]. The most familiar of those is the Lorentz line shape [18], [38]

$$F_L^i(f \pm f_c^i) = \frac{1}{\pi} \frac{\alpha_L^i}{(f \pm f_c^i)^2 + (\alpha_L^i)^2}. \tag{28}$$

This was enhanced by Van Vleck and Weisskopf in 1945 [38] and the Van Vleck-Weisskopf asymmetric line shape is defined as [38]–[40]

$$F_{VVW}^i(f) = \left(\frac{f}{f_c^i}\right)^2 [F_L^i(f - f_c^i) + F_L^i(f + f_c^i)]. \tag{29}$$

The Van Vleck-Weisskopf line shape with far end adjustments can be obtained as in [22]

$$F_{VVH}^i(f) = \frac{f}{f_c^i} \frac{\tanh(\frac{hf}{2k_BT})}{\tanh(\frac{hf_c^i}{2k_BT})} [F_L^i(f - f_c^i) + F_L^i(f + f_c^i)], \tag{30}$$

where h is Planck constant. This line shape has also been referred to as Van Vleck-Huber line shape due to derivation by Van Vleck and Huber [39]. In reality, the differences between these line shapes are rather small in the THz band and the choice of one over another does not produce large error.

At low pressures (below one kPa), i.e., in the higher altitudes, the Doppler broadening becomes the most significant broadening mechanism and it causes a Gaussian line shape [22]. The Doppler broadening half-width can be expressed as

$$\alpha_D^i = \frac{f_c^i}{c} \sqrt{\frac{2\log(2) k_B T}{m_i c^2}}, \tag{31}$$

where m_i is the molar mass of the absorbing species i. The Doppler line shape can be obtained as

$$F_D^i(f) = \sqrt{\frac{\log(2)}{\pi \alpha_D^i}} \exp\left(\frac{(f - f_c^i)^2 \log(2)}{c \alpha_D^i}\right). \tag{32}$$

The important thing here is which line shape to choose in the case of paths that penetrate vast vertical distances in the atmosphere. As we move from lower altitudes to higher altitudes, we need to decide which line shape is the appropriate one for calculating the line shape. In the transition zone, i.e., where Doppler and Lorentz half widths are comparable, one should utilize Voigt line shape [37]. This can be obtained as a convolution of the Lorentz and Doppler line shapes by

$$F_V^i(f) = \frac{1}{\sqrt{\pi}\alpha_D} \frac{1}{\pi} \frac{\alpha_L^i}{\alpha_D} \int_{\pm\infty} \frac{\exp(-t^2)}{[\frac{f - f_c}{\alpha_D} - t]^2 + (\frac{\alpha_L^i}{\alpha_D})} dt. \tag{33}$$

In our calculation, we utilize Voigt line shape for those lines that have Doppler and Lorentz half widths within five times of each other. Otherwise, the dominant line shape is utilized, i.e., the one that produces larger line width.

The line intensity S_0^i can be obtained from HITRAN database for reference temperature $T_0 = 296$ K, but it has to be scaled for the other temperatures with [41]

$$S^i(T) = S_0^i \frac{Q(T_0)}{Q(T)} \frac{e^{(-\frac{hcE_L^i}{k_B T})}}{e^{(-\frac{hcE_L^i}{k_B T_0})}} \left(\frac{1 - e^{(-\frac{hf_c^i}{k_B T})}}{1 - e^{(-\frac{hf_c^i}{k_B T_0})}}\right) \tag{34}$$

where E_L^i is the lower state energy of the transition of absorbing species i. Notice that we utilize HITRAN database where the lower state energies have been given in the units 1/cm. Thus, the multiplication of E_L^i with hc. The partition function $Q(T)$ and its definitions can be found in [41, Appendix A].

REFERENCES

[1] R. Piesiewicz *et al.*, "Short-range ultra-broadband terahertz communications: Concepts and perspectives," *IEEE Antennas Propag. Mag.*, vol. 49, no. 6, pp. 24–39, Dec. 2007.

[2] I. F. Akyildiz, J. M. Jornet, and C. Han, "Teranets: ultra-broadband communication networks in the terahertz band," *IEEE Wireless Commun.*, vol. 21, no. 4, pp. 130–135, Aug. 2014.

[3] M. Giordani, M. Polese, M. Mezzavilla, S. Rangan, and M. Zorzi, "Toward 6g networks: Use cases and technologies," *IEEE Commun. Mag.*, vol. 58, no. 3, pp. 55–61, Mar. 2020.

[4] T. S. Rappaport *et al.*, "Wireless communications and applications above 100 GHz: Opportunities and challenges for 6G and beyond," *IEEE Access*, vol. 7, pp. 78 729–78 757, 2019.

[5] ICAO, "The world of air transport in 2018," International Civil Aviation Organization Report, Tech. Rep., 2018. [Online]. Available: https://www.icao.int/annual-report-2018/Pages/the-world-of-air-transport-in-2018.aspx

[6] J. M. Jornet and I. F. Akyildiz, "Channel modeling and capacity analysis for electromagnetic nanonetworks in the terahertz band," *IEEE Trans. Wireless Commun.*, vol. 10, no. 10, pp. 3211–3221, Oct. 2011.

[7] B. Peng and T. Kürner, "Three-dimensional angle of arrival estimation in dynamic indoor terahertz channels using a forward-backward algorithm," *IEEE Trans. Veh. Technol.*, vol. 66, no. 5, pp. 3798–3811, May 2017.

[8] V. Petrov, J. Kokkoniemi, D. Moltchanov, J. Lehtomaki, Y. Koucheryavy, and M. Juntti, "Last meter indoor terahertz wireless access: Performance insights and implementation roadmap," *IEEE Commun. Mag.*, vol. 56, no. 6, pp. 158–165, 2018.

[9] S. Priebe, M. Kannicht, M. Jacob, and T. Kürner, "Ultra broadband indoor channel measurements and calibrated ray tracing propagation modeling at thz frequencies," *J. Commun. Netw.*, vol. 15, no. 6, pp. 547–558, 2013.

[10] V. Petrov *et al.*, "On unified vehicular communications and radar sensing in millimeter-wave and low terahertz bands," *IEEE Wireless Commun.*, vol. 26, no. 3, pp. 146–153, Jun. 2019.

[11] C. Han, A. O. Bicen, and I. F. Akyildiz, "Multi-ray channel modeling and wideband characterization for wireless communications in the terahertz band," *IEEE Trans. Wireless Commun.*, vol. 14, no. 5, pp. 2402–2412, May 2015.

[12] S. Priebe and T. Kürner, "Stochastic modeling of thz indoor radio channels," *IEEE Trans. Wireless Commun.*, vol. 12, no. 9, pp. 4445–4455, Sep. 2013.

[13] J. Y. Suen, M. T. Fang, S. P. Denny, and P. M. Lubin, "Modeling of terabit geostationary terahertz satellite links from globally dry locations," *IEEE Trans. Terahertz Sci. Technol.*, vol. 5, no. 2, pp. 299–313, Mar. 2015.

[14] J. F. Federici, J. Ma, and L. Moeller, "Review of weather impact on outdoor terahertz wireless communication links," *Nano. Commun. Netw.*, vol. 10, pp. 13–26, 2016, terahertz Communications. [Online]. Available: http://www.sciencedirect.com/science/article/pii/S1878778916300394

[15] Y. Balal and Y. Pinhasi, "Atmospheric effects on millimeter and submillimeter (thz) satellite communication paths," *J. Infrared, Millimeter, Terahertz Waves*, vol. 40, pp. 219–230, Mar. 2019.

[16] ITU, "Attenuation by atmospheric gases and related effects," Recommendation ITU-R P.676-12, Tech. Rep., Aug. 2019.

[17] ITU, "Radio noise," Recommendation, Tech. Rep. ITU-R P.372-14, Aug. 2019.

[18] S. Paine, "The *am* atmospheric model," Smithsonian Astrophysical Observatory, Cambridge, MA, USA, Tech. Rep. w152, version 11.0, Sep. 2019.

[19] A. Berk, P. Conforti, R. Kennett, T. Perkins, F. Hawes, and J. van den Bosch, "MODTRAN6: A major upgrade of the MODTRAN radiative transfer code," in *Algorithms Technol. Multispectral, Hyperspectral, and Ultraspectral Imagery XX*, M. Velez-Reyes and F. A. Kruse, Eds., vol. 9088, Int. Soc. Opt. Photon. SPIE, 2014, pp. 113–119. [Online]. Available: https://doi.org/10.1117/12.2050433

[20] J. R. Pardo, J. Cernicharo, and E. Serabyn, "Atmospheric transmission at microwaves (ATM): An improved model for millimeter/submillimeter applications," *IEEE Trans. Antennas Propag.*, vol. 49, no. 12, pp. 1683–1694, Dec. 2001.

[21] "NASA/NOAA's GOES Project," Mar. 2014. [Online]. Available: https://www.nasa.gov/content/three-atmospheric-dragons-low-pressure-areas-around-the-us/

[22] "Calculation of molecular spectra with the spectral calculator," [Online]. Available: https://www.spectralcalc.com/info/CalculatingSpectra.pdf

[23] J. Kokkoniemi, J. Lehtomäki, K. Umebayashi, and M. Juntti, "Frequency and time domain channel models for nanonetworks in terahertz band," *IEEE Trans. Antennas Propag.*, vol. 63, no. 2, pp. 678–691, Feb. 2015.

[24] ITU, "Specific attenuation model for rain for use in prediction methods," Recommendation, Tech. Rep. ITU-R pp. 838.3, Mar. 2005.

[25] ITU, "Attenuation due to clouds and fog," Recommendation, Tech. Rep. ITU-R P.840.8, Aug. 2019.

[26] ITU,"Propagation data and prediction methods required for the design of 979 of terrestrial line-of-sight systems," Recommendation, Tech. Rep. ITU-R P.530-17, Dec. 2017.

[27] T. L Wilson, "Introduction to millimeter/sub-millimeter astronomy," vol. 38. M. Dessauges-Zavadsky and D. Pfenniger Eds. Berlin, Heidelberg, Germany: Springer, Mar. 2018. [Online]. Available: https://doi.org/10.1007/978-3-662-57546-8_1ps://doi.org/10.1007/978-3-662-57546-8_1

[28] H. Nyquist, "Thermal agitation of electric charge in conductors," *Phys. Rev.*, vol. 32, pp. 110–113, Jul. 1928.

[29] "U.S. standard atmosphere 1976," NASA, Tech. Rep., NOAA-S/T-76-1562 Oct. 1976.

[30] "NASA EarthData GES DISC," [Online]. Available: https://disc.gsfc.nasa.gov/

[31] S. D. Slobin, "Microwave noise temperature and attenuation of clouds: Statistics of these effects at various sites in the United States, Alaska, and Hawaii," *Radio Sci.*, vol. 17, no. 6, pp. 1443–1454, Nov. 1982.

[32] S. U. Hwu, K. B. deSilva, and C. T. Jih, "Terahertz (THz) wireless systems for space applications," in *Proc. IEEE Sens. Appl. Symp. Proc.*, 2013, pp. 1–5,

[33] L. S. Rothman *et al.*, "The HITRAN 2008 molecular spectroscopic database," *J. Quant. Spectrosc. Radiat. Transfer*, vol. 110, no. 9–10, pp. 533–572, Jun.–Jul. 2009.

[34] N. Jacquinet-Husson *et al.*, "The 2009 edition of the GEISA spectroscopic database," *J. Quant. Spectrosc. Radiat. Transfer*, vol. 112, no. 15, pp. 2395–2445, Oct. 2011.

[35] H. M. Pickett, E. A. Cohen, B. J. Drouin, and J. C. Pearson, "Submillimeter, millimeter, and microwave spectral line catalog," 2003. [Online]. Available: http://spec.jpl.nasa.gov/ftp/pub/catalog/doc/catdoc.pdf

[36] R. T. Pierrehumbert, *Principles of Planetary Climate*. Cambridge, U.K.: Cambridge Univ. Press, 2010.

[37] X. Huang and Y. L. Yung, "A common misunderstanding about the voigt line profile," *J. Atmos. Sci.*, vol. 61, pp. 1630–1632, Jul. 2004.

[38] J. H. Van Vleck and V. F. Weisskopf, "On the shape of collision-broadened lines," *Rev. Mo.d. Phys.*, vol. 17, no. 2–3, pp. 227–236, 1945.

[39] J. H. Van Vleck and D. L. Huber, "Absorption, emission, and linebreadths: A semihistorical perspective," *Rev. Mod. Phys.*, vol. 49, no. 4, pp. 939–959, 1977.

[40] I. Halevy, R. T. Pierrehumbert, and D. P. Schrag, "Radiative transfer in CO_2-rich paleoatmospheres," *J. Geophys. Res.*, vol. 114, no. D18, pp. 1–18, Sep. 2009.

[41] L. S. Rothman *et al.*, "The HITRAN molecular spectroscopic database and HAWKS (HITRAN atmospheric workstation): 1996 edition," *J. Quant. Spectrosc. Radiat. Transfer*, vol. 60, no. 5, pp. 665–710, Nov. 1998.

Joonas Kokkoniemi (Member, IEEE) received the B.Sc. (Tech.), M.Sc. (Tech.), and Dr.Sc. (Tech.) degrees in communications engineering from the University of Oulu, Oulu, Finland, in 2011, 2012, and 2017, respectively. He is currently a Postdoctoral Research Fellow with Centre for Wireless Communications, the University of Oulu. From September to November 2013, he was a Visiting Researcher with the Tokyo University of Agriculture and Technology, Tokyo, Japan. From March to October 2017, he was a Visiting Postdoctoral Researcher with the State University of New York at Buffalo, Buffalo, NY, USA. His research interests include THz band and mmWave channel modeling and communication system's analysis.

Josep M. Jornet (Senior Member, IEEE) received the B.S. in telecommunication engineering, the M.Sc. in information and communication technologies in 2008 from Universitat Politecnica de Catalunya, Barcelona, Spain, and the Ph.D. degree in electrical and computer engineering from the Georgia Institute of Technology (Georgia Tech), Atlanta, GA, USA, in 2013. Between August 2013 and August 2019, he was a Faculty with the Department of Electrical Engineering, the University at Buffalo, The State University of New York, Buffalo, NY, USA. Since 2019, he has been an Associate Professor with the Department of Electrical and Computer Engineering, the Director of the Ultrabroadband Nanonetworking Laboratory and a Member of the Institute for the Wireless Internet of Things and the SMART Center, Northeastern University, Boston, MA, USA. He is currently the Lead PI on multiple grants from U.S. federal agencies, including the National Science Foundation, the Air Force Office of Scientific Research, and the Air Force Research Laboratory. He has authored or coauthored more than 160 peer-reviewed scientific publications, one book, and has also been granted four US patents in his research areas, which include terahertz communication networks, wireless nano-bio-communication networks, and the Internet of Nano-Things. Since July 2016, he has been a Editor-in-Chief of the *Nano Communication Networks Journal* (Elsevier). He was the recipient of the National Science Foundation CAREER Award and several other awards from IEEE, ACM, UB, and Northeastern University.

Vitaly Petrov (Member, IEEE) received the Specialist degree in information systems security from the Saint Petersburg State University of Aerospace Instrumentation, Saint Petersburg, Russia, the M.Sc. degree in IT and communications engineering, and the Ph.D. degree in communications engineering from the Tampere University of Technology, Tampere, Finland, in 2011, 2014, and 2020, respectively. Since 2020, he has been a Senior Standardization Specialist and a 3GPP RAN1 delegate with Nokia Bell Labs, Helsinki, Finland. In 2018, he was a Visiting Researcher with The University of Texas at Austin, Austin, TX, USA, in 2016 and 2019, a Visiting Researcher with University at Buffalo, The State University of New York, Buffalo, NY, USA, and in 2014, a Visiting Scholar with the Georgia Institute of Technology, Atlanta, GA, USA. His current research interests include mmWave and THz band communications, softwarized networks, cryptology, and network security. He was the recipient of the Best Student Paper Award at IEEE VTC-Fall 2015, the Best Student Poster Award at IEEE WCNC 2017, and the Best Student Journal Paper Award from IEEE Finland in 2019.

Yevgeni Koucheryavy (Senior Member, IEEE) received the Ph.D. degree from the Tampere University of Technology, Tampere, Finland, in 2004. He is currently a Professor and the Lab Director with the Unit of Electrical Engineering, Tampere University of Technology. He has authored or coauthored numerous publications in the field of advanced wired and wireless networking and communications. His current research interests include various aspects in heterogeneous wireless communication networks and systems, the Internet of Things and its standardization, and nanocommunications. He is an Associate Technical Editor of the *IEEE Communications Magazine* and the Editor of the IEEE COMMUNICATIONS SURVEYS AND TUTORIALS.

Markku Juntti (Fellow, IEEE) received the M.Sc. (EE) and Dr.Sc. (EE) degrees from the University of Oulu, Oulu, Finland, in 1993 and 1997, respectively.

From 1992 to 1998, he was with the University of Oulu. From 1994 to 1995, he was a Visiting Scholar with Rice University, Houston, TX, USA. From 1999 to 2000, he was a Senior Specialist with Nokia Networks, Oulu, Finland. Since 2000, he has been a Professor of communications engineering with the University of Oulu, Centre for Wireless Communications (CWC), where he leads the Communications Signal Processing Research Group. He is also the Head of CWC Radio Technologies (RT) Research Unit. He is also an Adjunct Professor with Department of Electrical and Computer Engineering, Rice University, Houston, TX, USA. He has authored or coauthored almost 500 papers published in international journals, conference records, and books *Wideband CDMA for UMTS* in 2000–2010, *Handbook of Signal Processing Systems* in 2013 and 2018 and *5G Wireless Technologies* in 2017. His research interests include signal processing for wireless networks and communication and information theory.

He was the Editor of IEEE TRANSACTIONS ON COMMUNICATIONS and an Associate Editor for IEEE TRANSACTIONS ON VEHICULAR TECHNOLOGY. He was the Secretary of IEEE Communication Society Finland Chapter in 1996–97 and the Chairman for years 2000–2001. He has been Secretary of the Technical Program Committee (TPC) of the 2001 IEEE International Conference on Communications (ICC), and the Chair or Co-Chair of the Technical Program Committee of several conferences including 2006 and 2021 IEEE International Symposium on Personal, Indoor and Mobile Radio Communications (PIMRC), the Signal Processing for Communications Symposium of IEEE Globecom 2014, Symposium on Transceivers and Signal Processing for 5G Wireless and mmWave Systems of IEEE GlobalSIP 2016, ACM NanoCom 2018, and 2019 International Symposium on Wireless Communication Systems (ISWCS). He was also the General Chair of 2011 IEEE Communication Theory Workshop (CTW 2011) and 2022 IEEE Workshop on Signal Processing Advances in Wireless Communications (SPAWC).